

Article

Hourly PM_{2.5} Estimation over Central and Eastern China Based on Himawari-8 Data

Yong Xue ^{1,2} , Ying Li ^{3,4,*}, Jie Guang ⁴, Alexandru Tugui ⁵, Lu She ⁴, Kai Qin ¹, Cheng Fan ⁴, Yahui Che ⁴, Yanqing Xie ⁴, Yanan Wen ⁴ and Zixiang Wang ⁴

¹ School of Environmental Science and Spatial Informatics, China University of Mining and Technology, No. 1 Daxue Road, Xuzhou 221116, China; Y.Xue@derby.ac.uk (Y.X.); qinkai@cumt.edu.cn (K.Q.)

² School of Electronics, Computing and Mathematics, College of Engineering and Technology, University of Derby, Kedleston Road, Derby DE22 1GB, UK

³ China Academy of Culture and Tourism, Beijing International Studies University, Beijing 100024, China

⁴ State Key Laboratory of Remote Sensing Science, Jointly Sponsored by the Institute of Remote Sensing and Digital Earth of Chinese Academy of Sciences and Beijing Normal University, Institute of Remote Sensing and Digital Earth, Chinese Academy of Sciences, Beijing 100094, China; guangjie@aircas.ac.cn (J.G.); shelu_wuhu@nxu.edu.cn (L.S.); fancheng@radi.ac.cn (C.F.); cheyh@radi.ac.cn (Y.C.); xieyq@radi.ac.cn (Y.X.); 15611670108@163.com (Y.W.); wangzixiang17@mails.ucas.ac.cn (Z.W.)

⁵ Faculty of Economy and Business Administration, Alexandru Ioan Cuza University, Iasi, Blvd. Carol I no. 11 Corp B, Et. II, B505, 700506 Iasi, Romania; altug@uaic.ro

* Correspondence: liying20190063@bisu.edu.cn

Received: 31 January 2020; Accepted: 5 March 2020; Published: 6 March 2020



Abstract: In this study, an improved geographically and temporally weighted regression (IGTWR) model for the estimation of hourly PM_{2.5} concentration data was applied over central and eastern China in 2017, based on Himawari-8 Advanced Himawari Imager (AHI) data. A generalized distance based on the longitude, latitude, day, hour, and land use type was constructed. AHI aerosol optical depth, surface relative humidity, and boundary layer height (BLH) data were used as independent variables to retrieve the hourly PM_{2.5} concentrations at 1:00, 2:00, 3:00, 4:00, 5:00, 6:00, 7:00, and 8:00 UTC (Coordinated Universal Time). The model fitting and cross-validation performance were satisfactory. For the model fitting set, the correlation coefficient of determination (R^2) between the measured and predicted PM_{2.5} concentrations was 0.886, and the root-mean-square error (RMSE) of 437,642 samples was only 12.18 $\mu\text{g}/\text{m}^3$. The tenfold cross-validation results of the regression model were also acceptable; the correlation coefficient R^2 of the measured and predicted results was 0.784, and the RMSE was 20.104 $\mu\text{g}/\text{m}^3$, which is only 8 $\mu\text{g}/\text{m}^3$ higher than that of the model fitting set. The spatial and temporal characteristics of the hourly PM_{2.5} concentration in 2017 were revealed. The model also achieved stable performance under haze and dust conditions.

Keywords: Himawari-8; AOD; PM_{2.5}; IGTWR; China; hourly

1. Introduction

Real-time monitoring of ground-level fine particulate matter (PM_{2.5}) concentrations is essential for the early warning of extreme weather events such as dust and haze, and the prediction of health exposure risks [1]. Satellite remote sensing with a large spatial coverage and continuous observations can address the limitations of ground-based monitoring [2–5] and provide comprehensive and reliable PM_{2.5} monitoring. Daily monitoring by polar orbit satellites cannot meet the requirements for real-time continuous monitoring. By contrast, the geostationary satellite Himawari-8 can provide high-frequency observations with broad coverage. Several aerosol retrieval methods based on Himawari-8 data have been developed [6–8]. Using an optimal estimation method, She et al. [9] successfully retrieved the

aerosol optical depth (AOD) from Himawari-8 data, and their algorithm estimated the hourly AOD over land with considerable accuracy.

Several algorithms have been developed to exploit the quantitative relationship between the AOD and $PM_{2.5}$ concentration, such as a semi-empirical model [10–13], multiple linear regression model [14], land use regression model [15], linear or nonlinear mixed effects model [16], generalized linear regression model [17], geographically weighted regression (GWR) model [18,19], and geographically and temporally weighted regression (GTWR) model [10]. There are some studies on the estimation of the hourly PM values using Himawari-8 aerosol property data, for example, studies on the estimation of the hourly $PM_{2.5}$ for the Beijing–Tianjin–Hebei region using a linear mixed-effect model [20] and the hourly $PM_{2.5}$ concentrations in Hebei using a vertical-humidity correction method [21]. The machine learning algorithm is also used to estimate hourly $PM_{2.5}$ over China [22,23]. However, research on hourly $PM_{2.5}$ data estimation for a large region of China based on the traditional statistical models is limited.

The least-squares method and GWR model were used to estimate $PM_{2.5}$ in the United States [24], over North America [18], and in China [19,25]. The GWR model is significantly more accurate than linear regression models. A GTWR model has been applied to MODIS/AOD data to calculate the ground-level $PM_{2.5}$ concentrations over China [26]. As the spatial and temporal variations should be considered simultaneously in the estimation of hourly $PM_{2.5}$ concentration data, a GTWR model is adopted in this study.

The PM monitoring network in China was built in 2012. Although monitoring stations of the network are located across the country, the distribution of the stations is spatially uneven. Most of them are located in central and eastern China, and only a few stations are present in the western part. Therefore, in this study, the hourly $PM_{2.5}$ data for central and eastern China, where extreme weather events such as haze and dust storms are frequent, were estimated. This paper describes the algorithm for retrieving the hourly $PM_{2.5}$ concentrations over central and eastern China using AOD data from the geostationary satellite Himawari-8. The selection of input parameters, calculation and setting of the key coefficients of the model, model structure composition, model performance, temporal and spatial distribution of hourly $PM_{2.5}$, and model testing under extreme weather conditions are also discussed.

2. Study Area and Data Sources

2.1. Study Area

This study focused on estimation of the hourly $PM_{2.5}$ data over central and eastern China. The study area (Figure 1, red boundary line) is located on the first and second steppes of China and has a varied topography, which increases the uncertainty in the estimation of $PM_{2.5}$. Therefore, we consider the full impact of the possible factors and select a suitable data set for the establishment of the model.

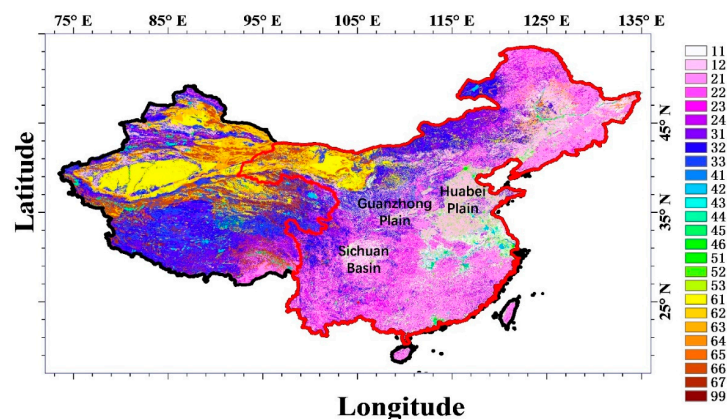


Figure 1. The distribution of land use types over China in 2015 [27]. The number of different land use types refers to the Land Use and Cover Change (LUCC) classification system, as shown in Table 1. The red boundary line represents the study area.

2.2. Data Sources

2.2.1. PM_{2.5} Data

The in situ ground-level PM_{2.5} concentrations are provided by the National Real-time Air Quality Publishing Platform (<http://106.37.208.233:20035/>). We collected hourly PM_{2.5} data for 1385 sites in the study area in 2017. The stations are relatively dense in urban areas, especially in the North China Plain, Northeast Plain, Yangtze River Delta, Guanzhong Plain, Pearl River Delta, and Sichuan Basin. The ground-based PM_{2.5} observation network provides sufficient data to support the construction of the PM_{2.5} remote sensing estimation model.

2.2.2. Himawari-8 Data

Level 1 (L1) data from the geostationary satellite Himawari-8 are officially provided by Japan's Meteorological Administration at resolutions of 2 and 5 km (<ftp.ptree.jaxa.jp>). When the atmospheric conditions remained relatively stable for an hour, we estimated the PM_{2.5} concentrations hourly. The L1 data used in this study were recorded at 1:00, 2:00, 3:00, 4:00, 5:00, 6:00, 7:00, and 8:00 UTC (Coordinated Universal Time). Himawari-8 Advanced Himawari Imager (AHI) AOD data were obtained using the joint retrieval algorithm for the surface reflectance and aerosol optical thickness proposed and implemented by She et al. [9].

2.2.3. Land Use Type

Notably, the land use types in adjacent areas may be different. For example, there are two different types of cultivated land, paddy fields and dry land, in eastern China. The underlying surface inevitably affects the relationship between the AOD and PM_{2.5}. This study mainly focuses on the effects of geographic distance, the type of underlying surface, the observation time, and other factors. The data on land use types in China in 2015 were provided by the Resource and Environment Data Cloud Platform (<http://www.resdc.cn/>) at a resolution of 10 km. These data were obtained via remote sensing interpretation methods, with human-computer interactions and visual interpretations based on Landsat 8 data [27]. Figure 1 shows the distribution of land use types in China in 2015. Table 1 describes the Land Use and Cover Change (LUCC) classification system. The land use types show the distribution of arable land, woodland, grassland, and desert from the east to the inland northwestern area.

Table 1. The land use types of LUCC classification system over China [27].

Number.	Land Use Type	Number	Land Use Type
11	Paddy field	45	Tidal flat
12	Dry land	46	Beach land
21	Woodland	51	Urban land use
22	Shrub woods	52	Rural settlements
23	Sparse woodland	53	Other developed land
24	Other woodlands	61	Sand
31	High-coverage grassland	62	Gobi
32	Medium-coverage grassland	63	Saline alkali soil
33	Low-coverage grassland	64	Swamp land
41	Channel	65	Bare land
42	Lake	66	Bare rock texture
43	Reservoir pond	67	Other
44	Permanent glacier and snow	99	Undefined

2.2.4. Relative Humidity

The relative surface humidity in central and eastern China varies greatly between 9:00 a.m. and 16:00 p.m. Beijing time. Atmospheric moisture plays an important role in the formation of secondary pollutants. Therefore, the humidity must be considered in PM estimations. The surface relative

humidity data used in this study are derived from Global Surface Summary of the Day observation data (<https://catalog.data.gov/dataset/global-surface-summary-of-the-day-gsod>). The temporal resolution is 30 min or 3 h depending on the site. First, we performed the temporal interpolation for each site. For each of the eight times from 9:00 a.m. to 16:00 p.m. Beijing time on one site, the closest relative humidity observation data before and after the time were extracted. The linear interpolation between the closed data extracted was used to obtain the relative humidity at each time. Then, we performed the spatial interpolation for each time. The surface relative humidity of each time was obtained via inverse distance-weighted interpolation between all the observation sites.

2.2.5. Boundary Layer Height

The boundary layer height has a notable effect on the atmospheric particulate matter concentrations [28]. The planetary boundary layer height used in this study was obtained from the ERA-2000 dataset released by the European Centre for Medium-Range Weather Forecasts (ECMWF), with a time resolution of 3 h. The BLH data on each site were extracted according to the ECMWF BLH value on its located pixel. The intraday hourly BLH was obtained by the linear interpolation between the closed data before and after each time. The intraday hourly BLH over central and eastern China was obtained via inverse distance-weighted interpolation between all the observation sites.

3. Improved Geographically and Temporally Weighted Regression Model

The geographic data are affected by both spatial and temporal factors. The geographically and temporally weighted regression model (GTWR) has been developed to solve the temporal and spatial problems (Equation (1)) [29]:

$$y_i = \beta_0(u_0, v_0, t_0) + \sum_{k=1}^d \beta_k(u_0, v_0, t_0)x_{ik} + \varepsilon_i, i = 1, 2, \dots, n. \quad (1)$$

In this function, i denotes the observation point ($i = 1, 2, \dots, n$, where n is the total number of observation points), k is a modelling parameter ($k = 1, 2, \dots, d$, where d is the total number of parameters), y_i is the estimated parameter, x_{ik} is the independent variable representing the value of k at point i , and β is the coefficient; u_0 , v_0 , and t_0 denote the longitude, latitude, and date, respectively, and ε_i represents the random error.

However, the estimation of surface level PM_{2.5} is not only affected by spatial–temporal factors, but also influenced by the underlying surface conditions. In this study, an improved geographically and temporally weighted regression (IGTWR) model was thereby established (Equation (2)). The parameters used in this model are AOD, RH, and BLH. The spatial (longitude and latitude), temporal (day and hour), and underlying surface data (land use data) are used to characterize the relationship between different sample sites.

$$y_i = \beta_0(u_0, v_0, d_0, h_0, l_0) + \beta_1(u_0, v_0, d_0, h_0, l_0)AOD_i + \beta_2(u_0, v_0, d_0, h_0, l_0)RH_i + \beta_3(u_0, v_0, d_0, h_0, l_0)BLH_i + \varepsilon_i, i = 1, 2, \dots, n. \quad (2)$$

Equation (2) can be written as Equation (3):

$$y_i = \beta_0(u_0, v_0, d_0, h_0, l_0) + \sum_{k=1}^d \beta_k(u_0, v_0, d_0, h_0, l_0)x_{ik} + \varepsilon_i, i = 1, 2, \dots, n. \quad (3)$$

In Equations (2) and (3), u_0 , v_0 , d_0 , h_0 , l_0 represent longitude, latitude, day, hour, and land use type, respectively. d refers to the number of independent variables (Himawari-8 AOD, relative humidity, and boundary layer height) in this model, and $d = 3$; i denotes the observation point, $i = 1, 2, \dots, n$, where n is the total number of observation points.

In this study, in order to calculate the weights of different sites in the regression process, the improved geographical and temporal weights $\omega_i(u_0, v_0, d_0, h_0, l_0)$ were introduced into the model. The weights were calculated using the longitude, latitude, day, hour, and land use type data for the 1385 observation stations in the study area. The Himawari-8 AOD, relative humidity, and boundary layer height data were used as independent variables to fit the concentration of PM_{2.5} over the study area. The objective function f is given by

$$f = \sum_{i=1}^n \left[y_i - \beta_0(u_0, v_0, d_0, h_0, l_0) - \sum_{k=1}^d \beta_k(u_0, v_0, d_0, h_0, l_0) x_{ik} \right]^2 \omega_i(u_0, v_0, d_0, h_0, l_0). \tag{4}$$

The regression objective is to find a set of coefficients that can minimize the objective function f . Assuming that a set of coefficients $\beta(u_0, v_0, d_0, h_0, l_0)$ can minimize the objective function according to the least-squares principle:

$$\beta(u_0, v_0, d_0, h_0, l_0) = [\beta_0(u_0, v_0, d_0, h_0, l_0) \ \beta_1(u_0, v_0, d_0, h_0, l_0) \ \dots \ \beta_d(u_0, v_0, d_0, h_0, l_0)]^T. \tag{5}$$

The partial derivative of the objective function f (Equation (4)) is computed, and the partial derivative with $\beta_r(u_0, v_0, d_0, h_0, l_0)$, $r = 0, 1, \dots, d$, is then set equal to 0, as follows:

$$\begin{aligned} \frac{\partial f}{\partial \beta_r(u_0, v_0, d_0, h_0, l_0)} &= -2 \sum_{i=1}^n [y_i - \beta_0(u_0, v_0, d_0, h_0, l_0) \\ &\quad - \sum_{k=1}^d \beta_k(u_0, v_0, d_0, h_0, l_0) x_{ik}] x_{ir} \omega_i(u_0, v_0, d_0, h_0, l_0) = 0. \end{aligned} \tag{6}$$

Equation (6) can be written as the following equation (Equation (7)):

$$\begin{cases} \frac{\partial f}{\partial \beta_0(u_0, v_0, d_0, h_0, l_0)} = -2 \sum_{i=1}^n \left[y_i - \beta_0(u_0, v_0, d_0, h_0, l_0) - \sum_{k=1}^d \beta_k(u_0, v_0, d_0, h_0, l_0) x_{ik} \right] \omega_i(u_0, v_0, d_0, h_0, l_0) = 0 \\ \frac{\partial f}{\partial \beta_1(u_0, v_0, d_0, h_0, l_0)} = -2 \sum_{i=1}^n \left[y_i - \beta_0(u_0, v_0, d_0, h_0, l_0) - \sum_{k=1}^d \beta_k(u_0, v_0, d_0, h_0, l_0) x_{ik} \right] x_{i1} \omega_i(u_0, v_0, d_0, h_0, l_0) = 0 \\ \vdots \\ \frac{\partial f}{\partial \beta_d(u_0, v_0, d_0, h_0, l_0)} = -2 \sum_{i=1}^n \left[y_i - \beta_0(u_0, v_0, d_0, h_0, l_0) - \sum_{k=1}^d \beta_k(u_0, v_0, d_0, h_0, l_0) x_{ik} \right] x_{id} \omega_i(u_0, v_0, d_0, h_0, l_0) = 0 \end{cases} \tag{7}$$

The next step is to solve the above equations (Equation (7)). Let W , Y , and X represent the following matrices:

$$W(u_0, v_0, d_0, h_0, l_0) = \text{diag}[\omega_1(u_0, v_0, d_0, h_0, l_0) \ \omega_2(u_0, v_0, d_0, h_0, l_0) \ \dots \ \omega_n(u_0, v_0, d_0, h_0, l_0)], \tag{8}$$

$$Y = \begin{bmatrix} y_1 \\ y_2 \\ \vdots \\ y_n \end{bmatrix}, \tag{9}$$

$$X = \begin{bmatrix} 1 & x_{11} & \dots & x_{1d} \\ 1 & x_{21} & \dots & x_{2d} \\ \vdots & \vdots & \ddots & \vdots \\ 1 & x_{n1} & \dots & x_{nd} \end{bmatrix}. \tag{10}$$

Then, Equation (7) can be expressed as follows:

$$[X^T W(u_0, v_0, d_0, h_0, l_0) X] \beta(u_0, v_0, d_0, h_0, l_0) = X^T W(u_0, v_0, d_0, h_0, l_0) Y. \tag{11}$$

The estimated value, $\hat{\beta}(u_0, v_0, d_0, h_0, l_0)$ (Equation (13)), of $\beta(u_0, v_0, d_0, h_0, l_0)$ at $(u_0, v_0, d_0, h_0, l_0)$ can be obtained by solving Equation (11) as follows (Equation (12)):

$$\hat{\beta}(u_0, v_0, d_0, h_0, l_0) = [X^T W(u_0, v_0, d_0, h_0, l_0) X]^{-1} X^T W(u_0, v_0, d_0, h_0, l_0) Y, \tag{12}$$

$$\hat{\beta}(u_0, v_0, d_0, h_0, l_0) = (\hat{\beta}_0(u_0, v_0, d_0, h_0, l_0) \hat{\beta}_1(u_0, v_0, d_0, h_0, l_0) \dots \hat{\beta}_d(u_0, v_0, d_0, h_0, l_0))^T. \tag{13}$$

The estimated PM_{2.5} concentration Y at $(u_0, v_0, d_0, h_0, l_0)$ is as follows:

$$\begin{aligned} \hat{y}(u_0, v_0, d_0, h_0, l_0) &= x_0^T \hat{\beta}(u_0, v_0, d_0, h_0, l_0) \\ &= x_0^T [X^T W(u_0, v_0, d_0, h_0, l_0) X]^{-1} X^T W(u_0, v_0, d_0, h_0, l_0) Y. \end{aligned} \tag{14}$$

Therefore, the PM_{2.5} concentration at $(u_i, v_i, d_i, h_i, l_i)$ is as follows:

$$\begin{aligned} \hat{y}(u_i, v_i, d_i, h_i, l_i) &= x_i^T \hat{\beta}(u_i, v_i, d_i, h_i, l_i) \\ &= x_i^T [X^T W(u_i, v_i, d_i, h_i, l_i) X]^{-1} X^T W(u_i, v_i, d_i, h_i, l_i) Y, \end{aligned} \tag{15}$$

and

$$x_i^T = (1 \ x_{i1} \ x_{i2} \ \dots \ x_{id}). \tag{16}$$

The selection of the weight coefficient $\omega_i(u_0, v_0, d_0, h_0, l_0)$ is particularly important for the regression model. The methods of calculating and selecting the weight coefficient $\omega_i(u_0, v_0, d_0, h_0, l_0)$ are described below.

The distance between the estimated points $(u_0, v_0, d_0, h_0, l_0)$ and any other observed sample data $(u_i, v_i, d_i, h_i, l_i)$ is defined as

$$d_{0i} = \sqrt{\lambda[u_0 - u_i]^2 + v_0 - v_i]^2 + \mu[d_0 - d_i]^2 + h_0 - h_i]^2 + \varphi[l_0 - l_i]^2}. \tag{17}$$

Here, λ , μ , and φ are the weight coefficients. The weight function $\omega_i(u_0, v_0, d_0, h_0, l_0)$ is expressed as a Gaussian function:

$$\begin{aligned} \omega_i(u_0, v_0, d_0, h_0, l_0) &= \exp\left(-\frac{d_{0i}^2}{h_{STL}^2}\right) \\ &= \exp\left\{-\frac{\lambda[(u_0 - u_i)^2 + (v_0 - v_i)^2] + \mu[d_0 - d_i]^2 + \varphi[(l_0 - l_i)^2]}{h_{STL}^2}\right\} \\ &= \exp\left\{-\left(\frac{\lambda[(u_0 - u_i)^2 + (v_0 - v_i)^2]}{h_{STL}^2} + \frac{\mu[d_0 - d_i]^2}{h_{STL}^2} + \frac{\varphi[(l_0 - l_i)^2]}{h_{STL}^2}\right)\right\} \\ &= \exp\left\{-\left(\frac{[(u_0 - u_i)^2 + (v_0 - v_i)^2]}{h_S^2} + \frac{[d_0 - d_i]^2}{h_T^2} + \frac{\varphi[(l_0 - l_i)^2]}{h_L^2}\right)\right\} \\ &= \exp\left\{-\left(\frac{(d_{0i}^S)^2}{h_S^2}\right)\right\} \times \exp\left\{-\left(\frac{(d_{0i}^T)^2}{h_T^2}\right)\right\} \times \exp\left\{-\left(\frac{(d_{0i}^L)^2}{h_L^2}\right)\right\} \\ &= \omega_i^S(u_0, v_0) \times \omega_i^T(d_0, h_0) \times \omega_i^L(l_0). \end{aligned} \tag{18}$$

Here, h_{STL} , h_S , h_T , and h_L are the bandwidths corresponding to the spatial (longitude and latitude), temporal (day and hour), and land use bandwidths, and $\omega_i^S(u_0, v_0)$, $\omega_i^T(d_0, h_0)$, and $\omega_i^L(l_0)$ are weights.

In this study, the cross-validation method [30] is used to select the optimal bandwidth and the optimal bandwidth that can provide the minimum residual:

$$CV(h_S, h_T, h_L) = \sum_{i=1}^n [y_i - \hat{y}_i(h_S, h_T, h_L)]^2, \tag{19}$$

$$CV(\hat{h}_S, \hat{h}_T, \hat{h}_L) = \min(CV(h_S, h_T, h_L)). \quad (20)$$

In this study, we used spatial, temporal, and underlying surface parameters to calculate the weight of different samples in the regression model. The hourly AHI AOD, BLH, and RH were used as independent variables to estimate the hourly surface level $PM_{2.5}$ over central and eastern China. The tenfold cross-validation was used as the $PM_{2.5}$ validation method. The model performance in the haze and dust event has also been evaluated and analyzed (Figure 2).

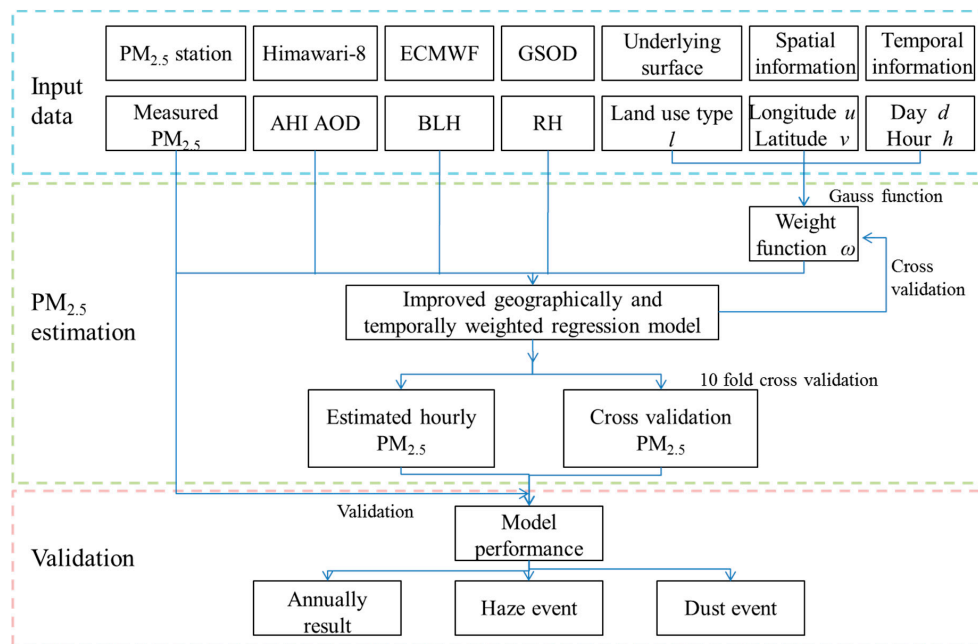


Figure 2. The model building and analysis strategy of the improved geographically and temporally weighted regression proposed in this study.

4. Results

4.1. Performance Evaluation of the IGTWR Model

In this study, the temporal, geographical, and underlying surface-weighted regression model was used to retrieve the ground-level $PM_{2.5}$ for 8 h per day during the daytime over central and eastern China in 2017. The hourly Himawari-8 AOD (1:00, 2:00, 3:00, 4:00, 5:00, 6:00, 7:00, and 8:00 UTC, which correspond to 9:00, 10:00, 11:00, 12:00, 13:00, 14:00, 15:00, and 16:00 Beijing time), surface relative humidity, and boundary layer height were selected as input parameters. The longitude, latitude, day, hour, and land use type were used to estimate the regression weight, and 437,642 samples were successfully matched and used as the modelling set to construct the GWR model. The model fitting performance is shown in Figure 3 (left). The tenfold cross-validation method was used to evaluate the model fitting (Rodriguez et al. 2010). We split the 437,642 matched data points evenly into ten parts. One part was used for validation, and the remaining nine parts were used for training. This process was repeated for every fold. The cross-validation results are shown in Figure 3 (right). For the 437,642 samples, the R^2 value between the predicted and observed $PM_{2.5}$ is 0.886, and the root-mean-square error (RMSE) of the model fit is only $12.180 \mu\text{g}/\text{m}^3$. In the scatterplot of the measured values versus the predicted values, the points are distributed around the 1:1 line. The correlation coefficient R^2 of the cross-validation is 0.784, and the RMSE is $20.104 \mu\text{g}/\text{m}^3$, which is only $8 \mu\text{g}/\text{m}^3$ higher than the RMSE of the model fit. The slope of the fitting line of the measured–predicted $PM_{2.5}$ scatter plot is 0.747, which indicates that the $PM_{2.5}$ was underestimated. However, for most sample points below $200 \mu\text{g}/\text{m}^3$, this underestimation is not obvious. The accuracy, reliability, and robustness of the $PM_{2.5}$ estimation under typical conditions are relatively high.

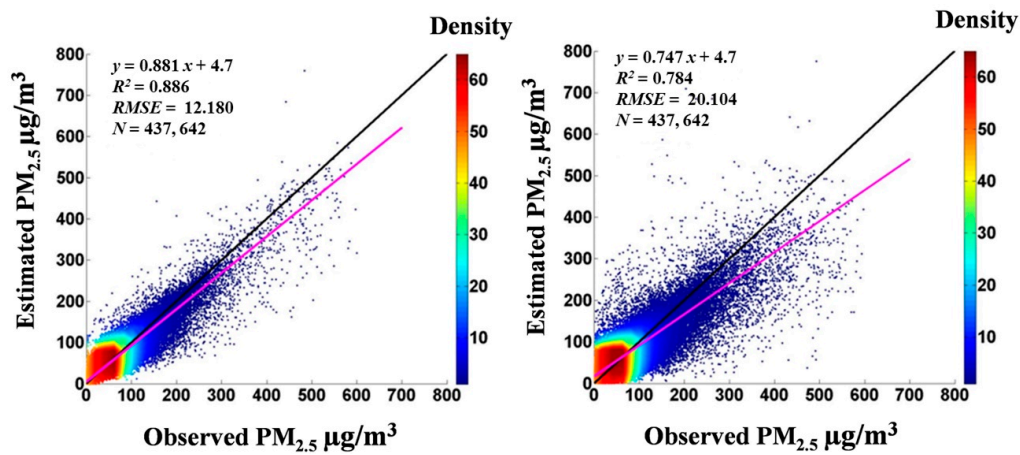


Figure 3. Scatter plots for (left) model fitting result and (right) tenfold cross-validation result. The color represents the sample density within a $10 \mu\text{g}/\text{m}^3$ radius.

4.2. Hourly $\text{PM}_{2.5}$ Concentration in Central and Eastern China

The hourly spatial distributions of $\text{PM}_{2.5}$ in the central and eastern parts of China are shown in Figure 4. The distribution of the 1385 sites is also shown in Figure 4 (second column from left). In addition, the annual $\text{PM}_{2.5}$ concentrations based on observational data are also shown in Figure 4. The annual average $\text{PM}_{2.5}$ concentration is below $100 \mu\text{g}/\text{m}^3$ for most of the study area. The spatial and temporal patterns of the estimated $\text{PM}_{2.5}$ concentrations are in agreement with the observed patterns.

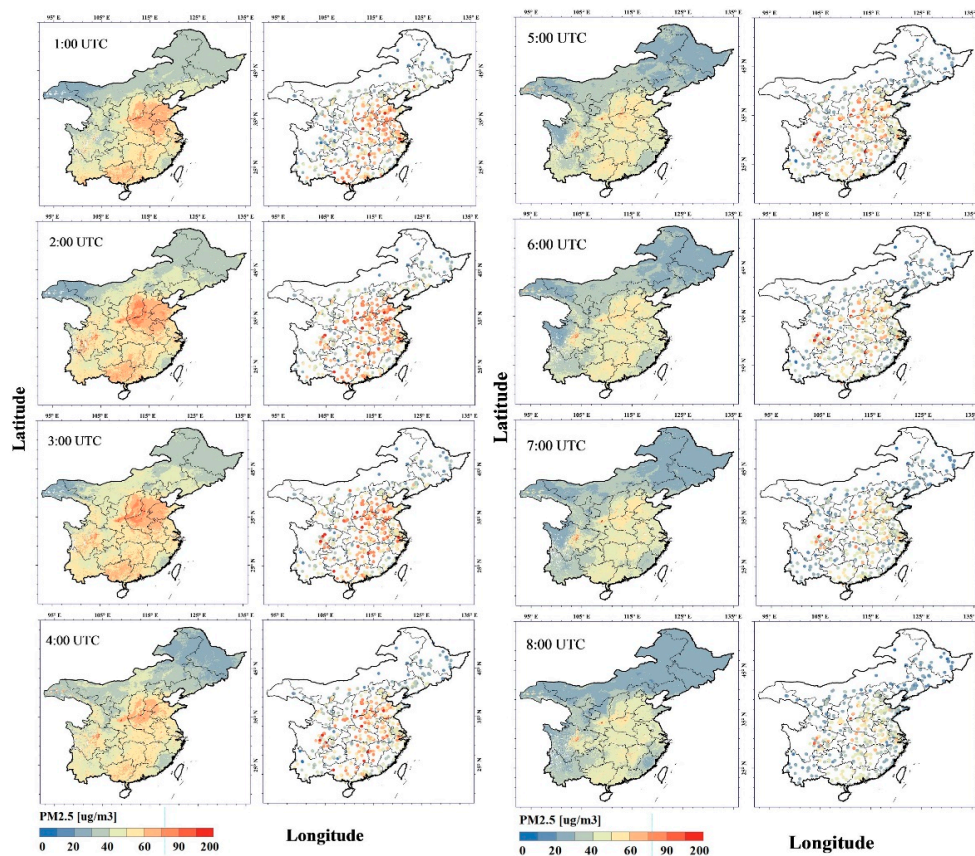


Figure 4. Annual average hourly $\text{PM}_{2.5}$ concentration in 2017. Columns 1 and 3 are the model estimation results, and columns 2 and 4 are the site observation data (the column number is 1, 2, 3, and 4 from left to right).

Spatially, severe atmospheric fine particulate matter pollution occurred mainly in the North China Plain, the Guanzhong Plain, the Fenwei Plain, the Yangtze River Delta, South China, and the Sichuan Basin. The fine particulate matter pollution in the North China Plain was extreme. An area of relatively stable and severe PM_{2.5} pollution formed in southern Hebei Province and northern Henan Province at the eastern foot of the Taihang Mountains owing to the effect of the mountains. Notably, the PM_{2.5} concentration in Beijing is even lower than that in the Yangtze River Delta and Pearl River Delta, which may be related to the air pollution measured in Beijing. The Atmospheric Environment Meteorological Bulletin also showed that the air quality values in Beijing, Tianjin, and Hebei improved continuously in 2017, and the annual number of haze pollution days dropped by 18.1. In southern China, for example, in Guangxi, the annual average concentration of fine particulate matter is more than 40–60 µg/m³. This result may be related to the unfavorable air diffusion conditions, such as temperature inversions, and the effects of biomass combustion in northern China and southern Asia [31].

Temporally, the PM_{2.5} concentrations in central and eastern China are higher in the morning and lower in the afternoon, and they tend to decrease gradually with time. Figure 4 shows that the highest concentration of PM_{2.5} occurred at 2:00 UTC. The annual mean concentration of PM_{2.5} in the main polluted areas is above 60 µg/m³ and then decreases gradually with time. At 8:00 UTC, the average PM_{2.5} concentration in the main polluted areas falls below 60 µg/m³. This variation in hourly PM_{2.5} may be closely related to the meteorological conditions. Before sunrise, the height of the atmospheric boundary layer is relatively low, and aerosols are concentrated in the lower level of the atmosphere, which results in a relatively high PM_{2.5} concentration near the surface. Then, with increasing solar altitude, the atmosphere is heated by solar radiation, which causes expansion and thermodynamic uplift, and the boundary layer rises accordingly [32,33]. The atmospheric particulate matter also moves to the upper atmosphere, resulting in a gradual decrease in the ground-level PM_{2.5} concentration. The geostationary satellite records this process perfectly. The Sichuan Basin is located in the southwest of China. The PM_{2.5} in the Sichuan Basin and other western areas obviously decreases at 5:00 UTC. The PM_{2.5} in the Huabei Plain and other eastern areas decreases after 3:00 UTC. The Sichuan Basin and the Huabei Plain are marked on Figure 1. It is very interesting that the decrease in PM_{2.5} in western China occurs later than in eastern China. Owing to the Earth's rotation, the western region of China receives solar radiation later than the eastern region, which delays the periodic change in PM_{2.5}. This phenomenon proves once again that the ground-level PM_{2.5} concentration is greatly affected by the solar radiation and atmospheric conditions. The intraday concentration of atmospheric fine particulate matter is not constant. Therefore, hourly monitoring of the PM_{2.5} concentration is necessary.

We selected 26 sites in central and eastern China as typical cities and calculated the annual PM_{2.5} concentration in 2017 (Figure 5). Differences between the estimated and observed PM_{2.5} concentrations in the selected 26 cities were analyzed. The PM_{2.5} concentrations were relatively high in Jinan, Hangzhou, Hefei, Zhengzhou, Xi'an, Taiyuan, and Chengdu. The measured and predicted PM_{2.5} concentrations in typical cities were in agreement except for those in Xi'an and Taiyuan. The underestimation of PM_{2.5} in Xi'an and Taiyuan is related to the great disparity of PM_{2.5} between rural and urban areas. As shown in the true color map of China in Figure 5, Xi'an and Taiyuan are located in the narrow plain or basin, which keeps pollution low-lying and stagnant. In addition, the intense human activities in urban areas also aggravate the air pollution. Xi'an and Taiyuan become the isolated PM_{2.5} hotspot that affected the performance of the model. From 1:00 to 8:00 UTC, the PM_{2.5} concentrations first increase and then decrease in nearly all the cities. The peak of the PM_{2.5} concentration appears earlier in eastern China than in western China, which is also consistent with our previous analysis. It is related to the influence of solar radiation. Due to the rotation of the Earth, the solar angle and intensity of radiation over eastern and central China is different. The boundary layer rises with the increase in solar radiation and carries the atmospheric particulate matter upward [32,33], and the ground-level PM_{2.5} concentrations decrease accordingly.

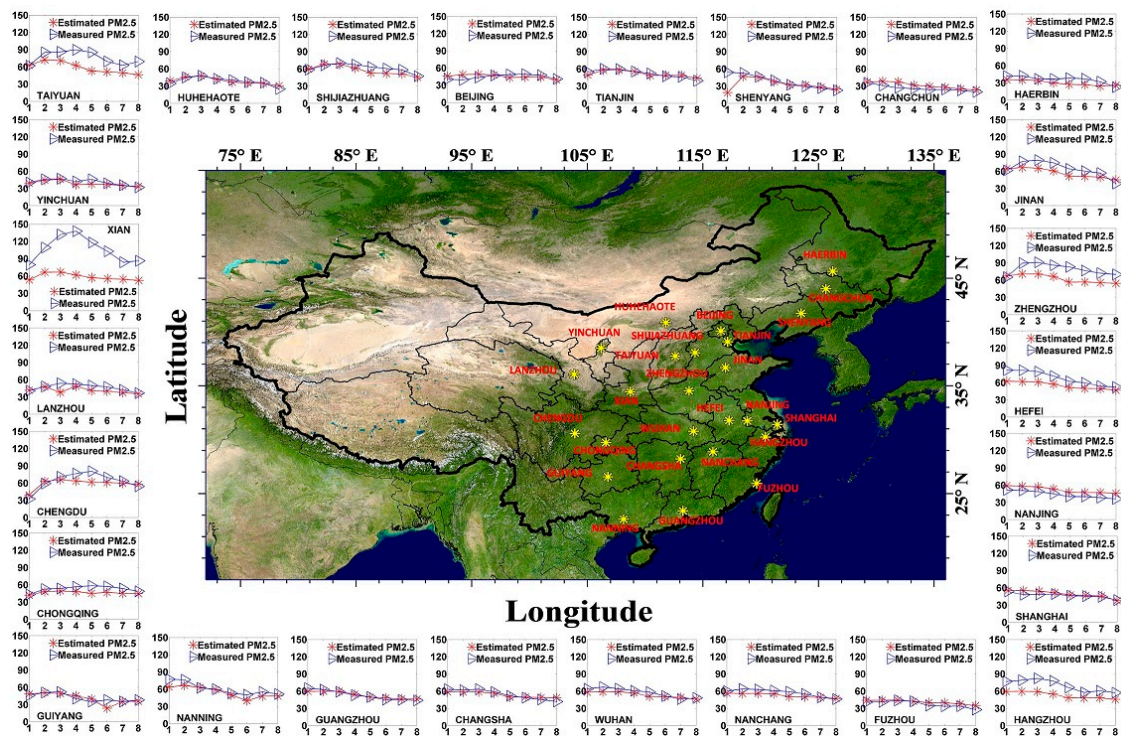


Figure 5. Annual average hourly $PM_{2.5}$ concentrations of 26 typical cities in 2017.

4.3. Model Performance in Typical Cases

The analysis in this section shows that the model is sensitive to the estimates of the ground-level hourly $PM_{2.5}$ concentrations. The model performance was tested for typical cases such as haze events and dust events.

4.3.1. Model Performance during Haze Events

A serious haze event occurred in South China on December 24, 2017. Based on the temporal, geographical, and underlying surface-weighted regression models, the $PM_{2.5}$ concentrations for 8 h on December 24, 2017 were estimated. The results are shown in Figure 6. The $PM_{2.5}$ estimation results were highly consistent with the monitoring data. The results show that haze occurred in Jiangxi, Hunan, Hubei, Anhui, Zhejiang, and Shanghai and that the $PM_{2.5}$ concentration exceeded $100 \mu\text{g}/\text{m}^3$. The $PM_{2.5}$ concentration was relatively high in the morning and then decreased gradually. The geostationary satellite retrieval results were also used to monitor the haze dissipation process. The $PM_{2.5}$ concentration began to decrease at 2:00 UTC in Anhui Province. Next, the haze in Zhejiang Province also began to dissipate. Although haze was still present in Jiangxi, Hunan, and Hubei provinces, the $PM_{2.5}$ concentration decreased. Until 7:00 UTC, the $PM_{2.5}$ concentration over the middle and lower reaches of the Yangtze River was below $70 \mu\text{g}/\text{m}^3$. In the middle and lower reaches of the Yangtze River on the 24th, the $PM_{2.5}$ concentration varied by more than $100 \mu\text{g}/\text{m}^3$ in 8 h. The geostationary satellite satisfied the requirements for continuous, real-time, and large-scale monitoring of $PM_{2.5}$ under these extreme weather conditions.

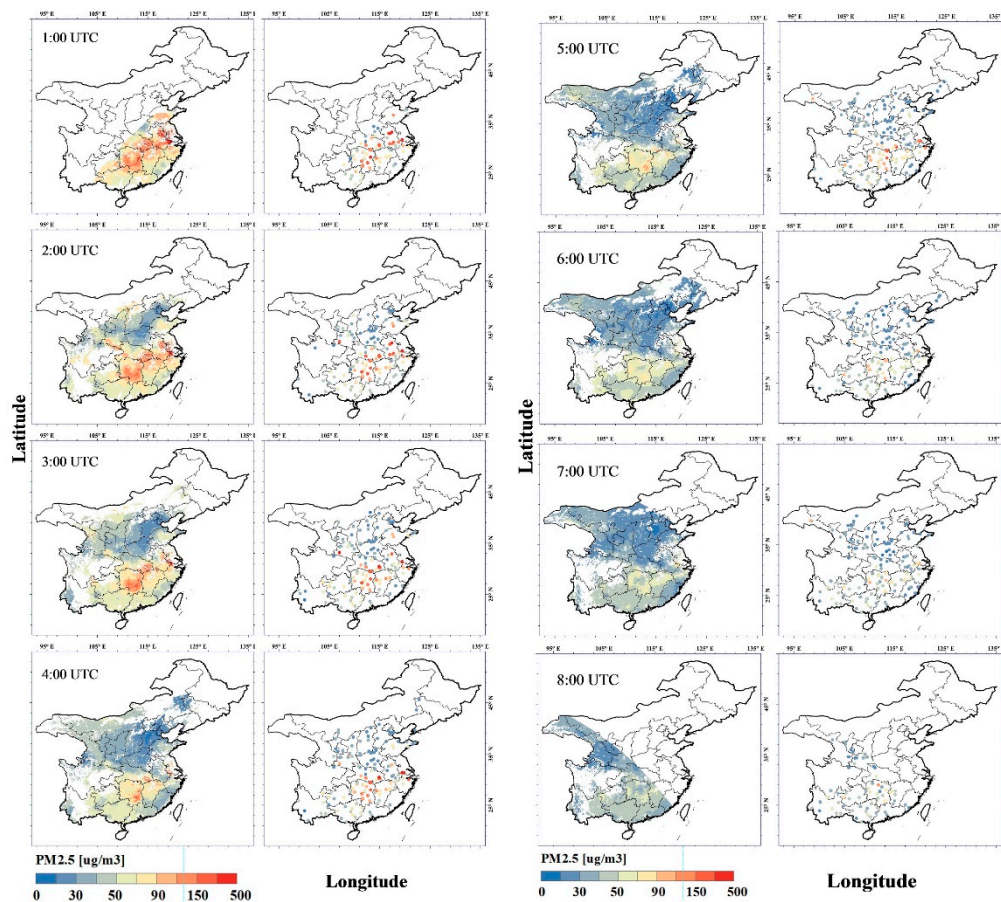


Figure 6. Predicted and observed $PM_{2.5}$ concentrations in study area during a haze event on December 24, 2017. Columns 1 and 3 are the model estimation results, and columns 2 and 4 are the site observation data (the column number is 1, 2, 3, 4 from left to right).

4.3.2. Model Performance during Dust Events

Dust storms are another weather event in which the $PM_{2.5}$ concentrations rise rapidly. An early warning and monitoring system for dust storms is particularly important. During severe dust storms, ground monitoring of $PM_{2.5}$ is often inaccurate owing to excessive wind speed and shows an abrupt increase in particulate matter concentration. This problem makes accurate monitoring of $PM_{2.5}$ concentrations difficult. However, geostationary satellites provide stable and continuous monitoring platforms that are not affected by extreme weather near the ground. The model's performance during dust events was also tested. Figure 7 shows a dust plume with a high $PM_{2.5}$ concentration that spreads from northwestern to northeastern China in May 2017. Dust was widespread in the north-central part of China. The $PM_{2.5}$ concentrations in Inner Mongolia, Southwestern Gansu, Ningxia, Northern Shaanxi, Shanxi, and Hebei provinces were more than $200 \mu\text{g}/\text{m}^3$. The geostationary satellite successfully captured the movement of the dust plume (Figure 7), which gradually moved from Inner Mongolia Province to Northeast China. The $PM_{2.5}$ concentration in western Inner Mongolia began to decrease gradually. After 6:00 UTC, the dust in western Inner Mongolia, southeastern Gansu, and Ningxia provinces began to weaken gradually. Until 8:00 UTC, the $PM_{2.5}$ concentration in the dust plume decreased to approximately $70 \mu\text{g}/\text{m}^3$. The effective ground-based $PM_{2.5}$ observation data were limited on May 4 and were concentrated mainly in the North China Plain. There were no ground monitoring data for Inner Mongolia, which was seriously affected by dust. The satellite-based $PM_{2.5}$ concentration estimation results are still highly consistent with the observation data.

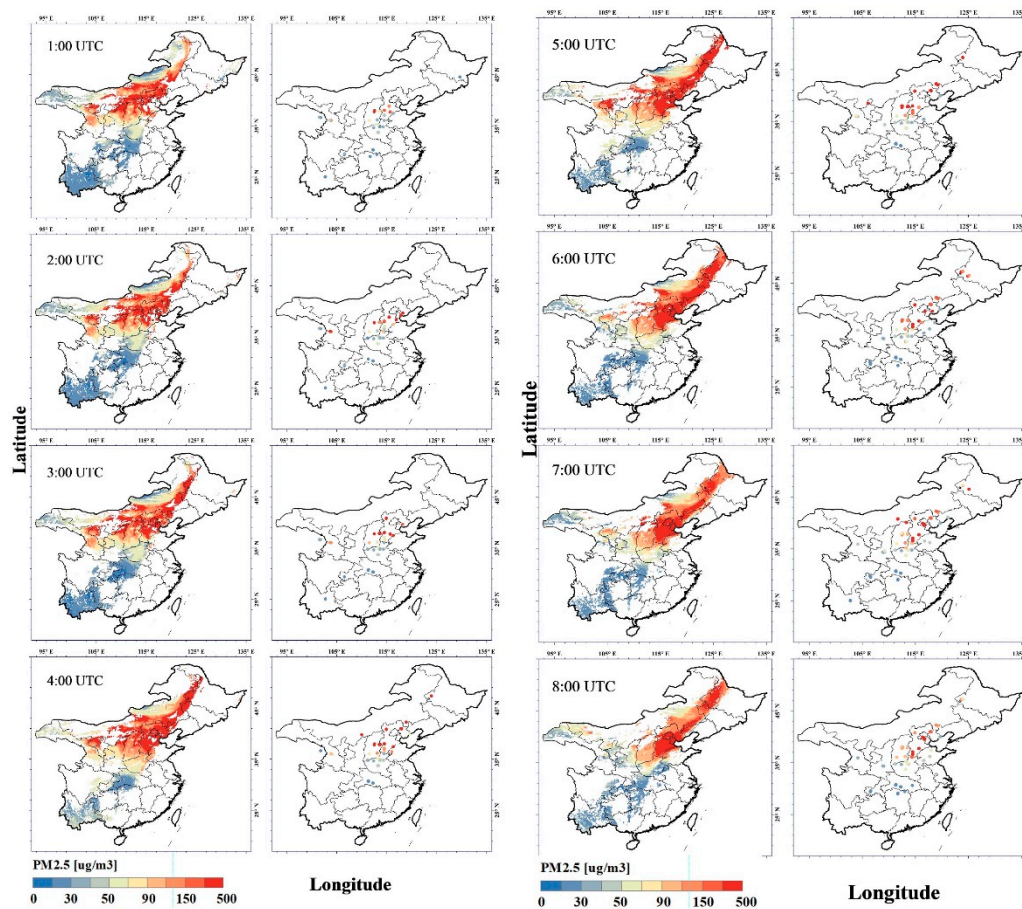


Figure 7. Predicted $PM_{2.5}$ concentrations in study area during a dust event on May 4, 2017. Columns 1 and 3 are the model estimation results, and columns 2 and 4 are the site observation data (the column number is 1, 2, 3, and 4 from left to right).

5. Discussion

The AHI AOD was calculated by a novel algorithm that uses a non-Lambertian forward model coupled with a surface bidirectional reflectance distribution function model. The accuracy of the retrieved AHI AOD is comparable to that of the MODIS AOD (C6). The coverage rate of the AHI AOD is better than that of the Japan Meteorological Agency (JMA)/AOD products [9].

Unlike the models used in previous studies, the IGTWR model generalized the geographical distance. Hu et al. [24] used the spatial distance as the weight parameter; later, Huang et al. [29] generalized this distance to a geographical and temporal distance by introducing the day number into the model. In this study, we also use the day, hour, and land use type to construct the distance. The R^2 value of the observed and predicted hourly $PM_{2.5}$ in our GTLWR fitting set is 0.886, and the RMSE is $12.18 \mu\text{g}/\text{m}^3$ for the 437,642 samples. In addition, the R^2 value of the observed and predicted daily $PM_{2.5}$ concentrations obtained by IGTWR is 0.87, and the RMSE is $14.56 \mu\text{g}/\text{m}^3$ for 60,810 samples in China. The IGTWR model still outperforms the GTWR model with a sample set that was approximately eight times larger.

In this study, ground-level hourly $PM_{2.5}$ concentrations in central and eastern China with high estimation accuracy were obtained. This achievement is meaningful for high-temporal-resolution air quality monitoring in China. Although the relevant research has been reported, which mainly focus on a relatively small region. Wang et al. [20] estimated the hourly $PM_{2.5}$ concentrations based on an improved linear mixed effects model for the Beijing–Tianjin–Hebei region with Himawari-8 data. The RMSE of the tenfold cross-validation result for the Beijing–Tianjin–Hebei region in that study

was $24.3 \mu\text{g}/\text{m}^3$ for 83,989 samples, whereas, in this study, we obtained the $\text{PM}_{2.5}$ validation result for central and eastern China with an RMSE of $12.18 \mu\text{g}/\text{m}^3$ for 437,642 samples.

The general spatial pattern of the hourly $\text{PM}_{2.5}$ pollution in China obtained by IGTWR is similar to that in previous studies [10,25], except that GTLWR shows that the Fenwei Plain becomes a $\text{PM}_{2.5}$ hotspot, and the North China Plain has lower $\text{PM}_{2.5}$ concentrations. The temporal characteristics of the satellite-based hourly $\text{PM}_{2.5}$ data in central and eastern China are also revealed. $\text{PM}_{2.5}$ showed an intraday decreasing trend, and the different performance in the eastern and western parts of our study area may be related to the timing of solar radiation [31].

The performance of the IGTWR model in extreme weather conditions, especially during dust events, is similar to the dust detection results reported in a previous study. She et al. [6] introduced an enhanced dust intensity index based on Himawari-8 brightness temperature data. The distribution of the hourly $\text{PM}_{2.5}$ concentration estimated by IGTWR on May 4, 2017 is consistent with the dust intensity index.

6. Conclusions

A temporally, geographically, and underlying surface weighted-regression model of the hourly $\text{PM}_{2.5}$ concentration was applied to central and eastern China in 2017. In this study, the weight of the generalized geographically weighted model was constructed using the longitude, latitude, day, hour, and land use type, and the AHI AOD, surface relative humidity, and boundary layer height data were used as independent variables. The hourly $\text{PM}_{2.5}$ concentrations in eastern and central China were estimated at eight times (1:00, 2:00, 3:00, 4:00, 5:00, 6:00, 7:00, and 8:00 UTC) in 2017.

The model fitting and cross-validation performance are satisfactory. For the modelling set, the R^2 value of the measured and predicted $\text{PM}_{2.5}$ is 0.886, and the RMSE is only $12.180 \mu\text{g}/\text{m}^3$. The tenfold cross-validation results of the regression model are also acceptable; the correlation coefficient R^2 of the measured and predicted $\text{PM}_{2.5}$ is 0.784, and the RMSE is $20.104 \mu\text{g}/\text{m}^3$, which is only $8 \mu\text{g}/\text{m}^3$ higher than that of the modelling set. The validation results showed highly predictable and reliable $\text{PM}_{2.5}$ estimation.

There are significant regional pollution characteristics over central and eastern China in 2017. Fine particulate matter pollution events are concentrated mainly in the North China Plain, Guanzhong Plain, Fenwei Plain, middle and lower reaches of the Yangtze River, South China, and Sichuan Basin. The ground-level $\text{PM}_{2.5}$ concentration is negatively correlated with the solar radiation. The predicted and measured values of the $\text{PM}_{2.5}$ concentration are highly consistent throughout the study area. The model results represent the actual distribution characteristics of $\text{PM}_{2.5}$ in central and eastern China.

The model designed in this study can monitor the occurrence, development, and termination of extreme weather events. The predicted $\text{PM}_{2.5}$ concentration is very similar to the observed $\text{PM}_{2.5}$ concentration. Satellite-based hourly $\text{PM}_{2.5}$ monitoring will play an important role in predicting extreme weather events and providing warnings in advance.

Author Contributions: Conceptualization, Y.X. and Y.L.; methodology, Y.L. and Y.X.; software, Y.C.; validation, J.G., Y.W. and Y.C.; formal analysis, Y.L. and L.S.; investigation, K.Q. and C.F.; resources, C.F. and Y.W.; data curation, A.T.; writing—Original draft preparation, Y.L.; writing—Review and editing, Y.X. and A.T.; visualization, Z.W.; supervision, Y.X.; project administration, J.G.; funding acquisition, Y.X. All authors have read and agreed to the published version of the manuscript.

Funding: This work was supported by the Ministry of Science and Technology (MOST) of China under grant no. 2016YFC02005 and the National Natural Science Foundation of China (NSFC) under grant nos. 41471260, 41471306 and 41590853.

Acknowledgments: This work was supported by the Ministry of Science and Technology (MOST) of China under grant no. 2016YFC02005 and the National Natural Science Foundation of China (NSFC) under grant nos. 41471260, 41471306 and 41590853. The data for analysis were obtained from JMA, ECMWF, the National Real-time Air Quality Publishing Platform, and the Resource and Environment Data Cloud Platform. We thank the investigators and their staffs for establishing and maintaining the important data used in this investigation.

Conflicts of Interest: The authors declare no conflict of interest.

References

1. Kloog, I.; Nordio, F.; Coull, B.A.; Schwartz, J. Incorporating local land use regression and satellite aerosol optical depth in a hybrid model of spatiotemporal PM_{2.5} exposures in the mid-atlantic states. *Environ. Sci. Technol.* **2012**, *6*, 11913–11921. [[CrossRef](#)] [[PubMed](#)]
2. Husar, R.B. Characterization of tropospheric aerosols over the oceans with the NOAA advanced very high resolution radiometer optical thickness operational product. *J. Geophys. Res.* **1997**, *102*, 16889–16909. [[CrossRef](#)]
3. Kahn, R.; Banerjee, P.; McDonald, D. Sensitivity of multiangle imaging to natural mixtures of aerosols over ocean. *J. Geophys. Res. Atmos.* **2001**, *106*, 18219–18238. [[CrossRef](#)]
4. Levy, R.C.; Remer, L.A.; Mattoo, S.; Vermote, E.F.; Kaufman, Y.J. Second-generation operational algorithm: Retrieval of aerosol properties over land from inversion of Moderate Resolution Imaging Spectroradiometer spectral reflectance. *J. Geophys. Res. Atmos.* **2007**, *112*. [[CrossRef](#)]
5. McGill, M.J.; Vaughan, M.A.; Trepte, C.R.; Hart, W.D.; Hlavka, D.L.; Winker, D.M.; Kuehn, R. Airborne validation of spatial properties measured by the CALIPSO lidar. *J. Geophys. Res. Atmos.* **2007**, *112*. [[CrossRef](#)]
6. She, L.; Xue, Y.; Yang, X.; Guang, J.; Li, Y.; Che, Y.; Fan, C.; Xie, Y. Dust detection and intensity estimation using himawari-8/AHI observation. *Remote Sens.* **2018**, *10*, 490. [[CrossRef](#)]
7. Zhang, W.; Xu, H.; Zheng, F. Aerosol optical depth retrieval over East Asia using himawari-8/AHI data. *Remote Sens.* **2018**, *10*, 137. [[CrossRef](#)]
8. Zhang, Z.; Fan, M.; Wu, W.; Wang, Z.; Tao, M.; Wei, J.; Wang, Q. A simplified aerosol retrieval algorithm for Himawari-8 advanced himawari imager over Beijing. *Atmos. Environ.* **2019**, *199*, 127–135. [[CrossRef](#)]
9. She, L.; Xue, Y.; Yang, X.; Leys, J.; Guang, J.; Che, Y.; Fan, C.; Xie, Y.; Li, Y. Joint retrieval of aerosol optical depth and surface reflectance over land using geostationary satellite data. *IEEE Trans. Geosci. Remote Sens.* **2019**, *57*, 1489–1501. [[CrossRef](#)]
10. He, Q.; Huang, B. Satellite-based mapping of daily high-resolution ground PM_{2.5} in China via space-time regression modeling. *Remote Sens. Environ.* **2018**, *206*, 72–83. [[CrossRef](#)]
11. Koелеmeijer, R.B.A.; Homan, C.D.; Matthijsen, J. Comparison of spatial and temporal variations of aerosol optical thickness and particulate matter over Europe. *Atmos. Environ.* **2006**, *40*, 5304–5315. [[CrossRef](#)]
12. Lin, C.; Li, Y.; Lau, A.K.H.; Deng, X.; Tse, T.K.T.; Fung, J.C.H.; Li, C.; Li, Z.; Lu, X.; Zhang, X.; et al. Estimation of long-term population exposure to PM_{2.5} for dense urban areas using 1-km MODIS data. *Remote Sens. Environ.* **2016**, *179*, 13–22. [[CrossRef](#)]
13. Zhang, Y.; Li, Z. Remote sensing of atmospheric fine particulate matter (PM_{2.5}) mass concentration near the ground from satellite observation. *Remote Sens. Environ.* **2015**, *160*, 252–262. [[CrossRef](#)]
14. Gupta, P.; Christopher, S.A. Seven year particulate matter air quality assessment from surface and satellite measurements. *Atmos. Chem. Phys. (ACP) Discuss. (ACPD)* **2008**, *8*, 3311–3324. [[CrossRef](#)]
15. Meng, X.; Fu, Q.; Ma, Z.; Chen, L.; Zou, B.; Zhang, Y.; Xue, W.; Wang, J.; Wang, D.; Kan, H.; et al. Estimating ground-level PM₁₀ in a Chinese city by combining satellite data, meteorological information and a land use regression model. *Environ. Pollut.* **2016**, *208*, 177–184. [[CrossRef](#)]
16. Lee, H.J.; Liu, Y.; Coull, B.A.; Schwartz, J.; Koutrakis, P. A novel calibration approach of MODIS AOD data to predict PM_{2.5} concentrations. *Atmos. Chem. Phys. (ACP) Discuss. (ACPD)* **2011**, *11*, 9769–9795. [[CrossRef](#)]
17. Liu, Y.; Sarnat, J.A.; Kilaru, V.; Jacob, D.J.; Koutrakis, P. Estimating ground-level PM_{2.5} in the Eastern United States using satellite remote sensing. *Environ. Sci. Technol.* **2005**, *39*, 3269–3278. [[CrossRef](#)]
18. van Donkelaar, A.; Martin, R.V.; Spurr, R.J.; Burnett, R.T. High-resolution satellite-derived PM_{2.5} from optimal estimation and geographically weighted regression over North America. *Environ. Sci. Technol.* **2015**, *49*, 10482–10491. [[CrossRef](#)]
19. You, W.; Zang, Z.; Zhang, L.; Zhang, M.; Pan, X.; Li, Y. A nonlinear model for estimating ground-level PM₁₀ concentration in Xi'an using MODIS aerosol optical depth retrieval. *Atmos. Res.* **2016**, *168*, 169–179. [[CrossRef](#)]
20. Wang, W.; Mao, F.; Du, L.; Pan, Z.; Gong, W.; Fang, S. Deriving Hourly PM_{2.5} Concentrations from Himawari-8 AODs over Beijing–Tianjin–Hebei in China. *Remote Sens.* **2017**, *9*, 858. [[CrossRef](#)]
21. Zeng, Q.; Chen, L.; Zhu, H.; Wang, Z.; Wang, X.; Zhang, L.; Gu, T.; Zhu, G.; Zhang, Y. Satellite-based estimation of hourly PM_{2.5} concentrations using a vertical-humidity correction method from Himawari-AOD in Hebei. *Sensors* **2018**, *18*, 3456. [[CrossRef](#)] [[PubMed](#)]

22. Chen, J.; Yin, J.; Zang, L.; Zhang, T.; Zhao, M. Stacking machine learning model for estimating hourly PM_{2.5} in China based on Himawari 8 aerosol optical depth data. *Sci. Total Environ.* **2019**, *697*, 134021. [[CrossRef](#)] [[PubMed](#)]
23. Liu, J.; Weng, F.; Li, Z.; Cribb, C.M. Hourly PM_{2.5} estimates from a geostationary satellite based on an ensemble learning algorithm and their spatiotemporal patterns over central east China. *Remote Sens.* **2019**, *11*, 2120. [[CrossRef](#)]
24. Hu, X.; Waller, L.A.; Al-Hamdan, M.Z.; Crosson, W.L.; Estes, M.G.; Estes, S.M.; Quattrochi, D.A.; Sarnat, J.A.; Liu, Y. Estimating ground-level PM_{2.5} concentrations in the southeastern U.S. using geographically weighted regression. *Environ. Res.* **2013**, *121*, 1–10. [[CrossRef](#)] [[PubMed](#)]
25. Ma, Z.; Hu, X.; Huang, L.; Bi, J.; Liu, Y. Estimating ground-level PM_{2.5} in China using satellite remote sensing. *Environ. Sci. Technol.* **2014**, *48*, 7436–7444. [[CrossRef](#)] [[PubMed](#)]
26. He, Q.; Geng, F.; Li, C.; Yang, S.; Wang, Y.; Mu, H.; Zhou, G.; Liu, X.; Gao, W.; Cheng, T.; et al. Long-term characteristics of satellite-based PM_{2.5} over East China. *Sci. Total Environ.* **2018**, *612*, 1417–1423. [[CrossRef](#)]
27. Xu, X.; Liu, J.; Zhuang, D. Remote sensing Monitoring methods of land use/cover changes in national scale. *J. Anhui Agric. Sci.* **2012**, *40*, 2365–2369. (In Chinese)
28. Miao, Y.; Liu, S.; Guo, J.; Huang, S.; Yan, Y.; Lou, M. Unraveling the relationships between boundary layer height and PM_{2.5} pollution in China based on four-year radiosonde measurements. *Environ. Pollut.* **2018**, *243*, 1186–1195. [[CrossRef](#)]
29. Huang, B.; Wu, B.; Barry, M. Geographically and temporally weighted regression for modeling spatio-temporal variation in house prices. *Int. J. Geogr. Inf. Sci.* **2010**, *24*, 383–401. [[CrossRef](#)]
30. Hastie, T.; Tibshirani, R. *Generalized Additive Models*; John Wiley & Sons, Inc.: Hoboken, NJ, USA, 1990.
31. Guo, Y.; Hong, S.; Feng, N.; Zhuang, Y.; Zhang, L. Spatial distributions and temporal variations of atmospheric aerosols and the affecting factors: A case study for a region in Central China. *Int. J. Remote Sens.* **2012**, *33*, 3672–3692. [[CrossRef](#)]
32. Guo, J.; Miao, Y.; Zhang, Y.; Liu, H.; Li, Z.; Zhang, W.; He, J.; Lou, M.; Yan, Y.; Bian, L.; et al. The climatology of planetary boundary layer height in China derived from radiosonde and reanalysis data. *Atmos. Chem. Phys.* **2016**, *16*, 13309–13319. [[CrossRef](#)]
33. Wang, L.; Gong, W.; Xia, X.; Zhu, J.; Li, J.; Zhu, Z. Long-term observations of aerosol optical properties at Wuhan, an urban site in Central China. *Atmos. Environ.* **2015**, *101*, 94–102. [[CrossRef](#)]



© 2020 by the authors. Licensee MDPI, Basel, Switzerland. This article is an open access article distributed under the terms and conditions of the Creative Commons Attribution (CC BY) license (<http://creativecommons.org/licenses/by/4.0/>).